Edge-Based Local and Global Energy Active Contour Model Driven by Signed Pressure Force for Image Segmentation

Asim Niaz, Ehtesham Iqbal, Asif Aziz Memon, Asad Munir, Jin Kim, and Kwang Nam Choi

***Abstract*— Image segmentation is a tedious task that suffers from constraints, such as blurred or weak edges and intensity inhomogeneity. Active contour models (ACMs), including edge- and region-based methods, are extensively used for image segmentation. Each of these methods has its pros and cons that affect image-segmentation accuracy and CPU processing time. This study combines local and global region-based fitting energies and uses statistical image information to drag contours toward object boundaries, thus overcoming image inhomogeneity. The bias field, the region affected by image artifacts, is calculated and added with the local fitting energy model to capture inhomogeneous object boundaries. Furthermore, the combined local and global statistical information is appended with the edge-indicator function to rapidly move the contour over objects with strong edges, thereby avoiding boundary leakage. A region-based length term is driven by the signed pressure force (SPF) function that evolves the curve on either the outer or inner side of the object, depending on its sign. The SPF function contributes to achieving a smoother version of energy minimization over gradient descent flow. The proposed ACM is applied to multiple synthetically generated, and medical images, together with online available public databases: the PH^2 database, the skin-cancer-mnist-ham10000 THUS10000 database, and the specific images from PascalVOC2007 database. All the experiments confirm the better segmentation accuracy and improved time potency of the proposed methodology over previous level set-based approaches.**

***Index Terms*— Active contours, bias field, image segmentation, inhomogeneous image segmentation, level set.**

I. Introduction

IMAGE segmentation is an important technique in image processing and computer vision, with many applications in different fields, such as medical image analysis [1], [2], intelligent transportation [3], [4], defect detection [5], and remote sensing [6]. The basic principle of image segmentation is to distinguish different objects in images. It is used to extract specific characteristics [regions of interest (ROIs)] from a given image for analysis. With the progress of artificial intelligence, a variety of image-segmentation technologies, such as deep neural networks [6], [7], [8], [9], [10] and scene parsing [11], [12], [13], [14], are developed in recent years. Such techniques belong to the category of learning-based methods; compared to traditional methods, they require more resources and data for searching statistical information and features [15]. Conventional methods, such as thresholding and unsupervised-based methods, are also important in the machine learning era. The active contour model (ACM), often termed the snake model, is based on an unsupervised method that was initially proposed by Kass et al. [16]. Since then, ACMs have remained one of the most used conventional methods for image segmentation. An active contour is a computer-generated curve guided by outer and inner forces that are further influenced by the image constraints. These forces attract contours toward image constraints such as edges and lines. Both forces evolve under the influence of partial differential equations (PDEs), which become zero at the object boundary. ACMs are divided into two different classes based on the image constraints: edge-based ACMs [17], [18], [19], [20], [21], [22] and region-based ACMs [23], [24], [25], [26], [27], [28], [29], [30], [31], [32], [33], [34], [35], [36], [37], [38], [39], [40], [41], [42], [43], [44], [45], [46], [47], [48]. Both types of ACMs have their strengths and weaknesses. Edge-based ACMs make use of a balloon force, consisting of image gradient information, to capture object boundaries. Such methods are useful for images with sharp object edges or boundaries and involve lower computational complexity. However, the performance of edge-based methods on images with blurred or weak edges is limited.

In contrast, region-based ACMs are independent of the image gradient and use region-based statistical information on the insides and outsides of the contour. Region-based ACMs are capable of segmenting objects with weak edges and are less accustomed to noise. Conventional region-based image-segmentation ACMs consider that overall image intensity is homogeneous, failing to catch the ROIs in the case of inhomogeneity in images. Overall, the edge-based ACMs perform effectively on images with a distinguishable difference between the ROI and the background. A classic case of region-based ACM is the Chan–Vese (C–V), an extension of the Mumford-Shah (M–S) ACM [49]. The C–V method

Manuscript received 1 May 2023; revised 1 August 2023; accepted 1 September 2023. Date of publication 13 November 2023; date of current version 15 November 2023. This work was supported in part by the Institute of Information and Communications Technology Planning and Evaluation (IITP) Grant funded by the Korean Government [Ministry of Science and ICT (MSIT)] (Development of the Technology to Automate the Recommendations for Big Data Analytic Models That Define Data Characteristics and Problems) under Grant 2020-0-00107 and in part by the "High Performance Computing (HPC) Support" Project through the Ministry of Science and Information and Communication Technology (ICT) and National IT Industry Promotion Agency (NIPA). The Associate Editor coordinating the review process was Dr. Chi-Hung Hwang. *(Corresponding author: Kwang Nam Choi.)*

Asim Niaz, Ehtesham Iqbal, and Kwang Nam Choi are with the Department of Computer Science and Engineering, Chung-Ang University, Seoul 06974, South Korea (e-mail: knchoi@vim.cau.ac.kr).

Asif Aziz Memon is with the Department of Computer Science and Engineering, Chung-Ang University, Seoul 06974, South Korea, and also with the Department of Computer Science, Dawood University of Engineering and Technology, Karachi 74800, Pakistan.

Asad Munir is with the Department of Industrial and Information Engineering, Università degli Studi di Udine, 33100 Udine, Italy.

Jin Kim is with SecuLayer, Inc., Seoul 04781, South Korea.

Digital Object Identifier 10.1109/TIM.2023.3317481

Fig. 1. Segmentation of an inhomogeneous image: (a) C-V model, (b) LBF model, and (c) LIF model column.

transforms the minimization problem into a curvature-flow problem [35]. This model effectively segments images with homogeneous objects of interest, but its performance is limited in that it produces unsatisfactory segmentation results on inhomogeneous images. This limitation arises from the general assumption in region-based methods that the images contain only homogeneous regions.

Real-world images are often affected by inhomogeneity, such as abrupt intensity variations, light effects, and low contrast. This limitation was overcome by Li et al. [50] presenting a local binary fitting (LBF) ACM using local image statistics and a Gaussian kernel deals with image inhomogeneity. This method is considerably limited by the initial contour position, leading to poor performance. Zhang et al. [28] presented their local image fitting (LIF) region-based ACM for inhomogeneous image segmentation. The LIF energy model extracts the local image information from the image and segments inhomogeneous images. A Gaussian kernel is employed to maintain a smooth contour evolution and avoid the reinitialization problem. Li et al. [50] dealt with intensity inhomogeneity by deriving the image local clustering property based on a local clustering criterion function. Fig. 1 shows the segmentation of an inhomogeneous object against a white background; local region-based ACMs perform better than global region-based models in the case of intensity corrupted images. Zhang et al. [51], [52] used bias field estimation in their model based on local fitting energies; this technique showed significant performance improvement on inhomogeneous images. In [51], a variational level set with bias correction (VLSBC) ACM is proposed with simultaneous bias field estimation and image segmentation. This model has also relied on the initial curve position. Oh et al. [32] presented a hybrid ACM, which combined the global region-based fitting term with the geodesic edge term, to perform image segmentation. The fractional varying-order differential (FVOD) model [53] introduced varying differential orders for different textural characteristics in an image, resulting in a new different image formulation and an energy functional for contour evolution. Despite a good alternative to previous work, converging PDEs of multiple orders adds to the computational cost of the FVOD. To overcome the limitations of previous ACMs, Wang et al. [48] proposed LPFBC ACM, which is a local pre-piecewise fitting bias correction model that utilizes an energy function and optimization techniques to achieve fast and accurate segmentation by minimizing the impact of image information grasp and model energy fluctuations.

Many deep learning-based approaches have been devised for image segmentation, including DeepLabV3+ [54], a famous segmentation model based on an encoder–decoder network. The encoder uses atrous convolution at various scales to capture multiscale contextual information, and the decoder effectively improves the segmentation results along object boundaries. Despite its state-of-the-art (SOTA) performance, it is a data-hungry model that requires massive amounts of labeled data; otherwise, it compromises its performance significantly, as further discussed in Section V. Contrarily, classic image-segmentation model, such as ACM, does not require labeled data and hence is less time-consuming as no time and labor costs associated with data labeling incur. [55]

Many research works, including [56], [57], [58], and [59], incorporated local energies with global energies to achieve superior performance than the previous methods. However, the difference is that each research has its unique energy functional formulation combining the local and global energies.

The proposed model combines local and global energies along with the edge-indicator function and the length-based region term with the signed pressure force (SPF) function in such a way that the contour fits the true boundary of the object of interest. The solution converges with higher accuracy and less computational time than previous methods.

Our literature review suggests that global-region-based ACMs are appropriate for images with homogeneous regions. Local-region-based ACMs are good at handling inhomogeneous images. The edge-based models are efficient over images with distinguishable differences between the background and the foreground. The ACMs with either local-region-based or global-region-based energy fitting terms only show limited performance for different levels of inhomogeneity.

This study aims to contribute to the scientific literature for image segmentation using ACMs. The principal contributions of this research are given as follows.

1) A novel fit model comprising both the local-region- and global-region-based image information to assist the moving contour in capturing objects of interest. The global-region-based image fitting energy helps speed up the contour evolution over homogeneous objects, while the local-region-based fitting energy confines contours over inhomogeneous object boundaries.
2) The inclusion of bias field estimation with the local-region-based fitting energy increases the accuracy of inhomogeneous image segmentation.
3) Appending the edge-indicator function with the fit model speeds up contouring over objects with strong edges.
4) A region-based length term, operated by the SPF function, helps the contour to suppress false contours and evolves either in the outer or inner direction depending on the force sign.

The implementation of the proposed methodology is followed by investigations comparing its results to other active contour-based models over several synthetically generated and real-world images. The experimental outcome affirms the superiority of the proposed edge-based local and global ACM operated with SPF function. Fig. 2 shows a graphical representation of the SPF function.

The rest of this article is organized as follows. Sections II and III comprise the previous works and the proposed methodology, respectively. Section IV illustrates and discusses briefly the experimental results that include segmentation quality analysis and ablation study, and Section V presents the discussion, followed by Section VI summarizing our study.

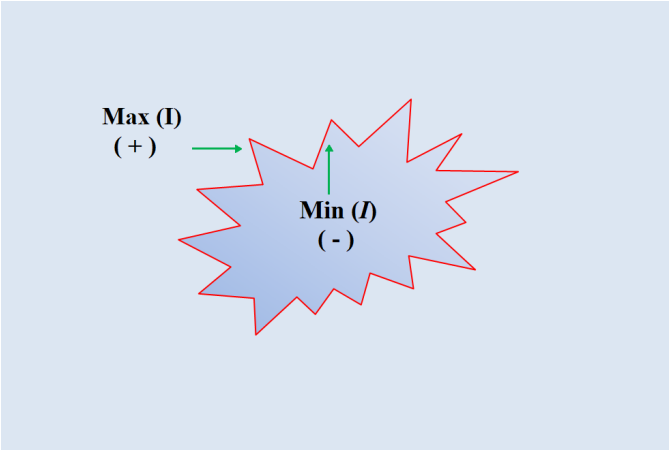

Fig. 2. Signs of the SPF function: SPF > 0 in the region outside the object boundary, SPF < 0 in the region inside the object boundary, and SPF $= 0$ at the object boundary.

II. Related Work

A. M-S Model

Consider Ω to be a bounded open subset of R^2 and $\partial\Omega$ to be the boundary of Ω. Let $I(x) \to R$ be the image under experiment and $C : [0, 1] \to R^2$ be a parameterized curve representing a contour.

The M-S model [49] is a basic region-based ACM. It achieves the solution image, I, by finding an optimal piecewise function, u, that varies within a subregion of the image domain in a smooth fashion. The proposed M-S energy functional is

$$E_{\mathrm{MS}}(I, C) = \lambda \int_{\Omega} (I - u)^2 dx + v \int_{\Omega \setminus C} (\nabla u)^2 dx + \mu \int_{\Omega} |C| \quad (1)$$

where $|C|$ shows the total length of the bounding contour C, and λ, v, and μ represent the positive-valued coefficients. M-S models show nonconvex behavior leading to irregularity of the edge term and make the energy minimization problem more complex.

B. C-V Model

Chan and Vese [35] proposed the C-V model, which is based on contour evolution approach and is inspired by one of the most basic and famous M-S models. The C-V model is the minimization of the energy-based segmentation model. Assume that two regions, outside (C) and inside (C), of appreciatively piecewise constant intensities form the input image $I(x)$.

The C-V model energy function is formulated as

$$\begin{aligned} E_{\mathrm{CV}}(C, c_1, c_2) &= \lambda_1 \int_{\mathrm{outside}(C)} |I(x) - c_1|^2 H_\epsilon(\phi(x)) dx \\ &\quad + \lambda_2 \int_{\mathrm{inside}(C)} |I(x) - c_2|^2 (1 - H_\epsilon(\phi(x))) dx \\ &\quad + \mu \int_{\Omega} |\nabla H_\epsilon(\phi(x))|^2 dx + v \int_{\Omega} H_\epsilon(\phi(x)) dx \end{aligned} \quad (2)$$

where c_1 and c_2 are the mean values of the global intensities from the outside(C) and inside(C) regions of image $I(x)$, respectively. λ_1, λ_2, and μ are parameters with values ≥ 0. The last and the second-to-last term in (2) represent the Euclidean length and the area of contour C, respectively. $H_\epsilon(\phi(x))$ is the regularized form of the Heaviside step function, which is expressed as

$$H_\epsilon(\phi(x)) = \frac{1}{2}\left(1 + \frac{2}{\pi} \arctan\left(\frac{\phi}{\epsilon}\right)\right). \quad (3)$$

ϵ regularizes the Heaviside function. c_1 and c_2 are expressed as

$$c_1 = \frac{\int_\Omega I(x) H_\epsilon(\phi(x)) dx}{\int_\Omega H_\epsilon(\phi(x))}, \quad c_2 = \frac{\int_\Omega I(x)(1 - H_\epsilon(\phi(x))) dx}{\int_\Omega (1 - H_\epsilon(\phi(x)))}. \quad (4)$$

The C-V model minimizes its energy function as a critical instance of the minimal partition problem. For (2), curve C evolves with respect to ϕ using [60] as

$$\frac{\partial \phi}{\partial t} = -\lambda_1 \delta_\epsilon(\phi)(I - c_1)^2 + \lambda_2 \delta_\epsilon(\phi)(I - c_2)^2 + \mu \delta_\epsilon(\phi) \mathrm{div}\left(\frac{\nabla \phi}{|\nabla \phi|}\right) - v \delta_\epsilon(\phi). \quad (5)$$

In (4), $\delta_\epsilon(x)$ represents a smooth form of the Dirac delta function, which is expressed as

$$\delta_\epsilon(\phi) = \frac{\epsilon}{\pi(\phi^2 + \epsilon^2)}. \quad (6)$$

The C-V model is proposed with the supposition of homogeneous image regions. It successfully segments images with homogeneous regions and can detect interior contours automatically. However, the performance efficiency of this region-based ACM is limited for inhomogeneous image-segmentation tasks.

C. LBF Model

Li et al. [50] encapsulated the local image information to propose their LBF energy function. The LBF method overcame the limitations of the C-V method and handled the inhomogeneous image-segmentation task with improved accuracy. Let $I(x) \subset R^2$ be a given image, $\phi : \Omega; R^2$ is the level set function, and C is the closed computer-generated line. The proposed LBF energy functional is expressed as

$$\begin{aligned} E_{\mathrm{LBF}}(C, f_1, f_2) &= \lambda_1 \int_\Omega K_\sigma(x - y)|I(y) - f_1(x)|^2 H_\epsilon(\phi(y)) dy \\ &\quad + \lambda_2 \int_\Omega K_\sigma(x - y)|I(y) - f_2(x)|^2 (1 - H_\epsilon(\phi(y))) dy \\ &\quad + \mu \int_\Omega \frac{1}{2}(\nabla \phi(x) - 1)^2 dx + v \int_\Omega \delta_\epsilon(\phi(x)) |\nabla \phi(x)| dx \end{aligned} \quad (7)$$

where λ_1 and λ_2 are the positive parameters and $H_\epsilon(\phi)$ is a smoother form of the Heaviside function defined in (3). $K_\sigma(x-y)$ represents a weighting function as a Gaussian kernel having a localization property. This property makes $K_\sigma(x-y)$ decrease and then reach zero as $|x - y|$ increases. $K_\sigma(x - y)$,

with a scaling parameter σ to control the region scalability, has the following mathematical representation:

$$K_\sigma(x-y) = \frac{1}{(2\pi)^{\frac{n}{2}}\sigma^n}\exp^{-\frac{|x-y|^2}{2\sigma^2}}. \tag{8}$$

In (8), f_1 and f_2 are the two numbers to fit the image intensities near the center point x of the above integral. In other words

$$f_1(x) = \frac{K_\sigma * [H_\epsilon(\phi)I(x)]}{K_\sigma * H_\epsilon(\phi)} \tag{9}$$

and

$$f_2(x) = \frac{K_\sigma * [(1-H_\epsilon(\phi))I(x)]}{K_\sigma * (1-H_\epsilon(\phi))} \tag{10}$$

are the local averages of the intensities from the insides and outsides of curve C, respectively. The gradient descent algorithm, from [60], minimizes (8) to

$$\begin{aligned}\frac{\partial\phi}{\partial t} &= -\lambda_1\delta_\epsilon(\phi)\int_\Omega K_\sigma(x-y)|I(x)-f_1(y)|^2dx \\ &\quad + \lambda_2\delta_\epsilon(\phi)\int_\Omega K_\sigma(x-y)|I(x)-f_2(y)|^2dx \\ &\quad + \upsilon\delta_\epsilon\mathrm{div}\left(\frac{\nabla\phi}{|\nabla\phi|}\right) + \mu\left(\nabla\phi - \mathrm{div}\left(\frac{\nabla\phi}{|\nabla\phi|}\right)\right).\end{aligned} \tag{11}$$

μ and υ are the scaling values for the distance regularization penalty term, and υ represents a positive parameter of the length term initiating the curve evolution toward object boundaries.

Though this model captures inhomogeneous objects in images, it sometimes fails to accomplish accurate segmentation. This method potentially traps into local minima that lead to false segmentation results.

D. LIF Model

Zhang et al. [28] introduced the LIF energy and used it to extract local image information to be used in achieving segmentation. Their model is capable of dealing with significant intensity inhomogeneity in images. The LIF model is based on Gaussian filtering as smoothing function to introduce their variational level set function. The LIF energy function is devised by keeping the difference between the original input image and the fit image minimized. The mathematical form is given as

$$E_{\mathrm{LIF}} = \frac{1}{2}\int_\Omega |I - I_{\mathrm{LIF}}|^2dx. \tag{12}$$

I_{LIF} in (12) accounts for local fit image formulation as

$$I_{\mathrm{LIF}}(x) = f_1(x)H_\epsilon(\phi) + f_2(x)(1-H_\epsilon(\phi)). \tag{13}$$

In (13), $f_1(x)$ and $f_2(x)$ account for the local mean intensities of the inside regions and the outside regions of point x, as defined by (9) and (10), respectively.

Using the gradient descent algorithm from [60], the energy functional (12) with respect to ϕ minimizes to

$$\frac{\partial\phi}{\partial t} = (I - I_{\mathrm{LIF}})(f_1(x) + f_2(x))\delta_\epsilon(\phi) \tag{14}$$

where $\delta(\phi)$ corresponds to the Dirac delta function expressed in (6). The computation time of the LIF model is less expensive and it is robust than the LBF model; however, it yields an analogous outcome.

E. VLSBC Model

Zhang et al. [51] presented a variational level set formulation for image segmentation and bias field estimation, also called a VLSBC model. They modeled intensity inhomogeneity to be Gaussian distributed with separate means and variances. They mapped the original image intensities onto other domains by introducing a sliding window. The mean Gaussian distributions, from the transformed domain, are adaptively estimated by multiplying a piecewise constant signal with the bias field. The region affected by the intensity corruption in images is called the bias field. The VLSBC model defines an energy functional on each local region combining the bias field with it. The energy formulation is given as

$$E_{\mathrm{VLSBC}} \approx \int\left(\Sigma_{i=1}\int_{\Omega i}^{N} K_\sigma(x-y)|I(y)-b(x)m_i|^2dy\right)dx. \tag{15}$$

This energy functional is the local clustering criteria function and is principled on an iterative k-means algorithm. The energy functional can further be minimized to

$$\begin{aligned}&E_{\mathrm{VLSBC}} \\ &= \int\left(\Sigma_{i=1}\int_{\Omega i}^{N} K_\sigma(x-y)|I(y)-b(x)m_i|^2M_i(\phi)dy\right)dx\end{aligned} \tag{16}$$

where M_i is the representation of the object region membership function with $x \in \{\Omega_i\}_{i=1}^N$. m_i accounts for the intensity means for distinguished regions, ω_i, where $i = 1, 2, 3, \ldots, i$; m_i is given as

$$m_i = \int \frac{K_\sigma * (I(x)b(x)M_i(\phi))}{K_\sigma * \left(b(x)^2M_i(\phi)\right)} \tag{17}$$

where $b(x)$ is the bias field, which is estimated as

$$b(x) = \Sigma_{i=1}^N \frac{K_\sigma * (I(x)m_iM_i(\phi))}{K_\sigma * \left(m_i^2M_i(\phi)\right)}. \tag{18}$$

This VLSBC model is motivated by the retinex model; it defines an inhomogeneous image as

$$I(x) = b(x)J(x) + n(x) \tag{19}$$

where $n(x)$ is the additive noise and

$$J(x) \approx \Sigma_{i=1}^N m_iM_i(\phi) \tag{20}$$

is the true image, free from inhomogeneous intensity corruption. The VLSBC model is relatively robust, but it lags in performance for some cases.

F. FRAGL Model

Fang et al. [61] proposed the fuzzy region-based active contours driven by weighting global and local fitting energy (FRAGL) model by incorporating fuzzy sets with combined local and global energy functions. FRAGL energy functional is given as

$$E_{\mathrm{FRAGL}} = E^{\mathrm{rg}} + E^{\mathrm{edg}} \tag{21}$$

where E^{rg} is the fuzzy region-based energy function and

$$E^{edg} = r_1 L(u - 0.5) + r_2 P(u - 0.5) \tag{22}$$

is the edge-based energy function. r_1 and r_2 are positive terms and

$$L = \int_\Omega \delta(u - 0.5)|\nabla(u - 0.5)|dx \tag{23}$$

and

$$P = \frac{1}{2}\int_\Omega 1 - |\nabla(u - 0.5)|dx \tag{24}$$

are the regularization terms and penalty terms, respectively. Overall, the FRAGL model produces acceptable results as can be observed in Section IV.

G. FVOD Model

Zhang and Tian [53] proposed their FVOD model based on the idea that not all pixels in an image are of similar texture; therefore, the same differential order is insufficient for effective contour evolution. The FVOD model carries out different differential orders for pixels of different textural characteristics. The FVOD model processes a new difference image $(I(x)_{new})$ as the input image, formulated as

$$I(x)_{new} = I(x) + \text{mag}(D_A I(x)) \tag{25}$$

where

$$\text{mag}(D_A I(x)) = |(D_{Ax} I(x))| + |(D_{Ay} I(x))| \tag{26}$$

is the fractional varying-order gradient magnitude and D_{Ax} and D_{Ay} are the fractional varying-order partial derivatives, respectively; for deeper understanding, see [53].

FVOD energy final functional is given as

$$E_{FVOD} = E_{VLSBC} + \upsilon E_R + \mu E_P \tag{27}$$

where E_{VLSBC} is taken from (16), but with new difference image $(I(x)_{new})$ as the input image

$$E_R = \int |\nabla H(\phi)|dx \tag{28}$$

and

$$E_P = \int p(|\nabla\phi|)dx \tag{29}$$

are the contour length and the penalty terms, respectively. The calculations for PDEs of multiple orders add to the computational cost of this method.

III. Proposed Method

This section presents the formulation of an edge-based local and global ACM driven with spf function. For image segmentation using level sets, image information, such as intensity, inhomogeneity level, edges, or texture, could help increase segmentation quality. The level set is basically the solution of numeric changes in image topology. This is obvious that relying only on the global perspective of image is insufficient for effective contour evolution, especially when image intensities are not homogeneous. The proposed method combines statistical information of the local and global image regions to drag contours toward the objects to be segmented. This information is further embedded with the edge indicating function to capture ROIs accurately in images. Furthermore, the spf function-based length term forces contours to stick robustly to the ROI boundaries.

Consider that $I(x) : \Omega \subset R^2 \to R$ is the given image; the proposed edge-based local and global energy ACM equation is

$$E_{ELGS} = E_{ELG} + \mu L_t extspf(\phi) \tag{30}$$

where E_{ELG} is the proposed energy term combining the edge-based local and global statistical information. $L_t extspf(\phi)$ is the region-based length term driven by the spf function, which minimizes the possibility of sticking into local minima. The length term increases the influence of interior and exterior forces of the contour, helping faster propagation of the function toward object boundaries. μ is the width controlling constant for the Dirac delta function. The energy function E_{ELG} is given as

$$E_{ELG}(\phi) = \int_\Omega g(\nabla(I))(I - I_{cbLFE})(I - I_{GFE})dx \tag{31}$$

where $g(\nabla(I))$ is the edge-indicator function with positive decreasing fashion [21], which is defined as

$$g(\nabla(I)) = \frac{1}{1 + |\nabla G_\sigma * I(x)|}. \tag{32}$$

This edge-indicator function is used here to approximate the edge intensities taking smaller values at the object boundary, where $g \in [0, 1]$. I_{GFE} is the global fitting energy model, which is defined as

$$I_{GFE} = \upsilon_1 M_1 + \upsilon_2 M_2 \tag{33}$$

and I_{cbLFE} is the local fitting energy model convolved with a Gaussian kernel for computational efficiency, which is defined as

$$I_{cbLFE} = G(x) * (b(x)(m_1 M_1 + m_2 M_2)) \tag{34}$$

where m_1 and m_2 represent local mean intensities and $b(x)$ is the bias field accountable for image intensity corruption, defined by (17) and (18), respectively. M_1 and M_2 stand for membership functions with relations $H(\phi)$ and $(1 - H(\phi)$, respectively. In (35), υ_1 and υ_2 are the global intensity means of the inner and outer regions of the curve, respectively, inspired by (4), and defined by appending the edge-indicator function as

$$\upsilon_1 = \frac{\int_\Omega I(x)g(\nabla(I))H_\epsilon(\phi(x))dx}{\int_\Omega g(\nabla(I))H_\epsilon(\phi(x))}$$
$$\upsilon_2 = \frac{\int_\Omega I(x)g(\nabla(I))(1 - H_\epsilon(\phi(x)))dx}{\int_\Omega g(\nabla(I))(1 - H_\epsilon(\phi(x)))}. \tag{35}$$

$L_t extspf(\phi)$, the region-based length term, is defined as

$$L_t extspf(\phi) = \int_\Omega textspf(I)\delta_\epsilon(\phi)|\nabla\phi| \tag{36}$$

where spf is the SPF function modulating the contour evolution sign $[-1, 1]$ inside and outside the contour such that it attracts and expands itself when inside and outside the ROI, respectively. The spf function is given as

$$textspf(I) = \frac{I(x) - I_{GFE}(x)}{\max(|I(x) - I_{GFE}(x)|)}. \tag{37}$$

TABLE I
PARAMETERS SETTINGS

Parameter	Name	Value
Δt	Time rate	0.01
p	Initial level set	2
σ	Gaussian kernel	2.5
ϵ	Dirac constant	1.5

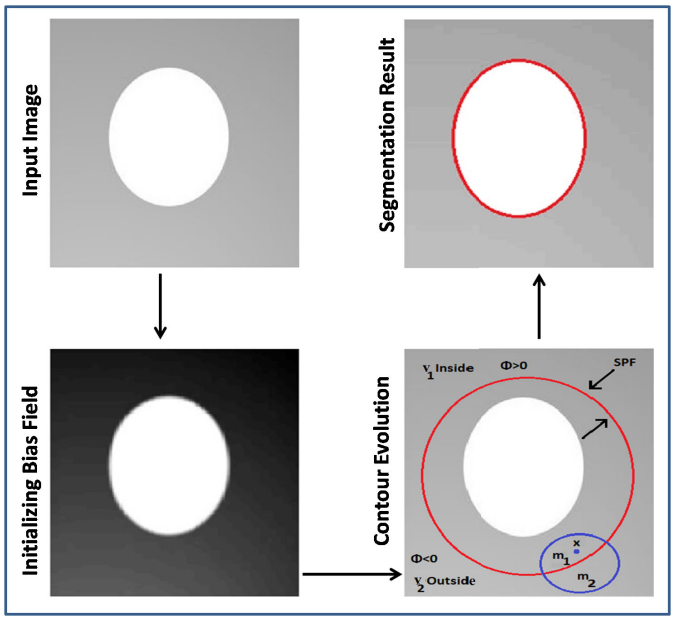

Fig. 3. Visual representation of the proposed methodology. The proposed methodology is an edge-based local and global ACM driven by an SPF function, combining local and global image information for more effective contour evolution and accurate segmentation, particularly in images with nonhomogeneous intensities.

The global-region-based models are insufficient to segment inhomogeneous images; therefore, we combine them with local-region-based models to effectively overcome this limitation. An edge-indicator function, appended with the local and global energy functions, contributes to capturing the ROI boundaries robustly. The SPF function assists in suppressing false contour appearances in the image-segmentation results, expanding the correctness of the contour evolution strategy.

Applying calculus of variation [60], the numeric solution of the proposed ACM equation minimizes to

$$\begin{aligned}\frac{\partial \phi}{\partial t} &= \delta_\epsilon(\phi)\mu \mathrm{div}\left(textspf(I)\frac{\nabla(\phi)}{|\nabla(\phi)|}\right) \\ &\quad + g(\nabla(I)(I(x) - I_{\mathrm{cbLFE}}(x))(v_1 - v_2) \\ &\quad \times (I(x) - I_{\mathrm{GFE}}(x))(f_1 - f_2)\delta_\epsilon(\phi). \end{aligned} \tag{38}$$

Table I shows the optimal parameter settings for generating results in this study.

Fig. 3 shows the visual representation of the proposed method. The proposed ACM takes an input image, estimates the bias field, calculates local and global energies, appends them with the gradient flow and evolves itself under the influence of an spf.

The proposed approach is summarized in Algorithm 1 as an iterative algorithm.

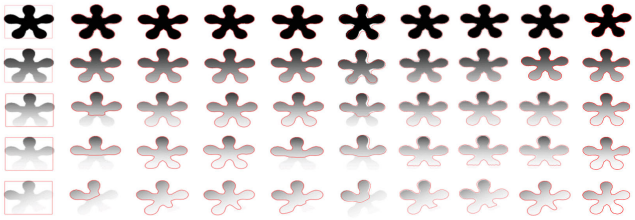

Fig. 4. Segmentation results over a single-object synthetic image with multiple levels of inhomogeneity. Column 1: input images with initial contours. Column 2: C-V [35]. Column 3: LBF [50]. Column 4: LIF [28]. Column 5: VLSBC [51]. Column 6: Zhang et al. [52]. Column 7: FVOD [53]. Column 8: FRAGL [61]. Column 9: SAM [62]. Column 10: proposed model.

Algorithm 1 Proposed Approach in an Iterative Algorithmic Form

1 Initializing bias field from $b_0 = 1$.
2 Initialization of level set ϕ from $t = 0$,

$$\phi_{t=0} = \begin{cases} -p, & x \in \Omega_0 - \partial\Omega_0 \\ 0, & x \in \partial\Omega_0 \\ p, & x \in \Omega - \partial\Omega_0 \end{cases} \tag{39}$$

where c is constant, Ω shows the image domain with Ω_0 subset, and $\partial\Omega_0$ represents the starting contour boundary.
3 Initialize iteration count, $m = 0$.
4 Compute local and global intensity means m_1, m_2 and v_1, v_2 from (17) and (35), respectively.
5 Compute spf using (37).
6 Update bias field from (18).
7 Solve PDE (38) in ϕ to get $\phi_{(t+1)}$.
8 Check for convergence.
- If not, then update $m = m + 1$, recall steps 4–7.
- If converged: stop the contour evolution.

IV. EXPERIMENTS AND RESULTS

This section compares the outputs of the different ACMs with the proposed image-segmentation model. Multiple synthetic, real, and medical images are used to test the proposed model and conduct segmentation experiments.

We used MATLAB 2018a with a 3.40-GHz Intel Core i7 and 8 GB of random access memory.

Fig. 4 presents the segmentation results of a single-object synthetic image with multiple levels of inhomogeneity. Column 1 represents original input images, followed by results of C-V [35], LBF [50], LIF [28], VLSBC [51], Zhang et al. [52], FVOD [53], FRAGL [61], SAM [62], and the proposed model. All the ACMs successfully segmented ROIs in the first and second rows, while the C-V model [35] and the model proposed by Zhang et al. [52] show poor performance in the third row. In the fourth row, only the LIF [28] and the proposed model completely captured the inhomogeneous object. Except for the proposed model, all other models failed to capture the object in the last row. This comparison shows the robustness of the proposed methodology and confirms that it is the most accurate among all the methods compared. Table II presents the CPU times and iterations for contour evolution over the

TABLE II

CPU TIMES AND ITERATIONS FOR CONTOUR EVOLUTION OVER THE IMAGES IN FIG. 4

Method		Row 1	Row 2	Row 3	Row 4	Row 5
CV[37]	Time (s)	1.97	2.41	3.47	4.56	5.34
	Iterations	100	100	100	500	500
LBF [45]	Time (s)	7.43	7.89	8.38	9.54	11.63
	Iterations	500	500	500	500	500
LIF [32]	Time (s)	0.98	1.23	1.67	1.97	2.34
	Iterations	80	100	150	500	500
VLSBC [46]	Time (s)	1.02	2.87	2.87	3.21	4.04
	Iterations	50	50	50	50	70
Zhang et al. [47]	Time (s)	3.76	3.87	3.98	4.53	4.62
	Iterations	50	50	50	70	100
FVOD [52]	Time (s)	2.05	2.18	2.32	2.48	2.67
	Iterations	50	50	50	50	50
FRAGL [60]	Time (s)	1.05	1.55	1.62	1.78	1.97
	Iterations	10	20	30	45	50
SAM [61]	Time (s)	1.37	1.59	1.68	1.74	1.87
	Iterations	8	10	13	15	15
Proposed Model	Time (s)	0.87	0.90	0.94	1.09	1.17
	Iterations	2	3	3	4	5

TABLE III

CPU TIMES AND ITERATIONS FOR CONTOUR EVOLUTION OVER THE IMAGES IN FIG. 5

Method		Row 1	Row 2
C-V	Time (s)	7.4	1.89
	Iterations	500	50
LBF	Time (s)	9.21	4.74
	Iterations	26	40
LIF	Time (s)	5.64	4.0
	Iterations	500	200
VLSBC	Time (s)	1.42	3.13
	Iterations	50	50
Zhang et al.	Time (s)	1.37	8.64
	Iterations	50	50
FVOD	Time (s)	2.23	2.43
	Iterations	50	50
FRAGL	Time (s)	1.09	1.45
	Iterations	10	15
SAM	Time (s)	1.29	1.86
	Iterations	10	10
Proposed Model	Time (s)	0.93	1.03
	Iterations	2	4

different images in Fig. 4. Table II confirms the time efficiency of the proposed model.

Fig. 5 compares the results produced by the different ACMs. The top row shows the results of a synthetic image having multiple objects; all the methods produce similar results in this case. In the second row, segmentation results over a synthetic hand image are presented. Almost all the ACMs captured the ROI without showing false contours except the LIF [28] model. The LIF [28] model was also able to distinguish boundaries between the middle fingers. However, only the SAM [62] and the proposed model captured the distinguished boundaries between all the fingers without false contours. Table III lists the CPU times and iterations for contour evolution over the images in Fig. 5. Table III confirms the time efficiency of the proposed method.

Fig. 5. Segmentation results over synthetic images. Column 1: input images. Column 2: C-V [35]. Column 3: LBF [50]. Column 4: LIF [28]. Column 5: VLSBC [51]. Column 6: Zhang et al. [52]. Column 7: FVOD [53]. Column 8: FRAGL [61]. Column 9: SAM [62]. Column 10: proposed model.

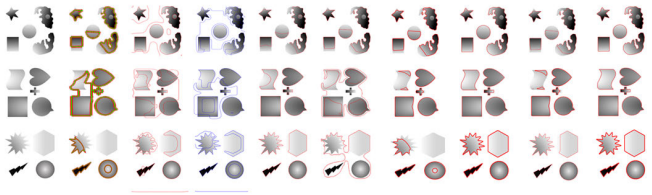

Fig. 6. Segmentation results over synthetic images with multiple inhomogeneous objects. Column 1: input images. Column 2: C-V [35]. Column 3: LBF [50]. Column 4: LIF [28]. Column 5: VLSBC [51]. Column 6: Zhang et al. [52]. Column 7 FVOD [53]. Column 8: FRAGL [61]. Column 9: SAM [62]. Column 10: proposed model.

Fig. 6 shows the segmentation results of various computer-generated images, each having multiple objects, affected by inhomogeneity. The first column contains the input (given) images, which is followed by the segmentation result images of the C-V [35], LBF [50], LIF [28], VLSBC [51], Zhang et al. [52], FVOD [53], FRAGL [61], SAM [62], and the proposed method in the subsequent columns. Fig. 6 highlights the instability of the previous ACMs with respect to segmentation accuracy. The C-V [35] model fails to capture ROIs due to its assumption of homogeneous intensity. LBF [50] and LIF [28] show better performance, but they produce false contour lines. VLSBC [51] and FRAGL [61] can suppress false contour lines, yet they fail at finding accurate boundaries of ROIs in the case of inhomogeneous objects. Moreover, FVOD [53] and the SAM [62] struggle as the inhomogeneity increases. However, the proposed ACM achieves segmentation accuracy superior to all the previous models. Table IV summarizes the CPU times and iterations for contour evolution over the images in Fig. 6. Table IV confirms the time efficiency of the proposed method.

Fig. 7 shows the representation of results generated by various methods, including the proposed method, over real images. Row 1 contains given images, followed by the results of C-V [35], LBF [50], LIF [28], VLSBC [51], Zhang et al. [52], FVOD [53], FRAGL [61], SAM [62], and the proposed method. The LBF [50] model captured object boundaries along with false contours. The FRAGL [61] method generates reasonable segmentation in the third column image, while it fails to suppress false contour appearances in the second image. The LIF method [28] and the method proposed by Zhang et al. [52] show limited performance as the contours are limited to the local minima. The VLSBC [51], FVOD [53], and SAM [62] model show acceptable results with the limitation of a nonsmooth object boundary compared to our method, whereas the proposed method outperforms previous ACMs in terms of segmentation results and time efficiency. Table V represents the statistical information of methods involved in the segmentation results of Fig. 7. Table V confirms the time efficiency of the proposed model.

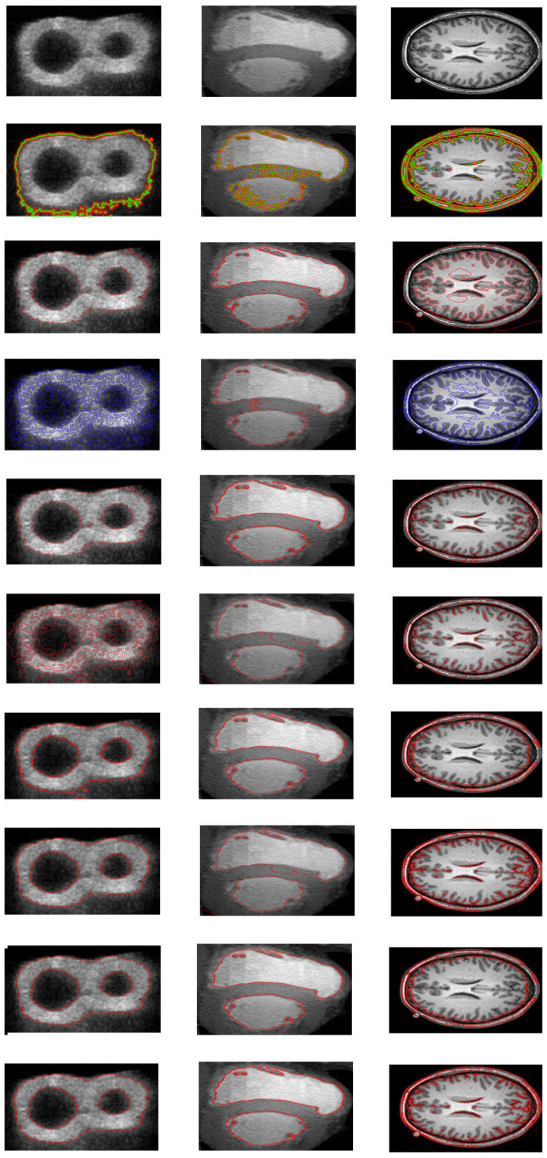

Fig. 7. Segmentation results over real images. Row 1: input images. Row 2: C-V [35]. Row 3: LBF [50]. Row 4: LIF [28]. Row 5: VLSBC [51]. Row 6: Zhang et al. [52]. Row 7: FVOD [53]. Row 8: FRAGL [61]. Row 9: SAM [62]. Row 10: proposed model.

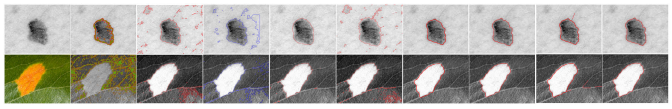

Fig. 8. Segmentation results over real images. Column 1: input images. Column 2: C-V [35]. Column 3: LBF [50]. Column 4: LIF [28]. Column 5: VLSBC [51]. Column 6: Zhang et al. [52]. Column 7: FVOD [53]. Column 8: FRAGL [61]. Column 9: SAM [62]. Column 10: proposed model.

Fig. 8 represents the segmentation results of various ACMs on two different real images. The image in the top row is corrupted with sudden intensity variations and inhomogeneity. In the first row, the C-V [35] captured the object boundary, but the appearance of false contours, although in lower quantities compared with LBF [50], LIF [28], and the method proposed by Zhang et al. [52], reduces its performance. FRAGL [61] performs well with slightly lower accuracy than the proposed model. In the second row, C-V [35] fails to capture the ROI, whereas LBF [50] and LIF [28] detected the object boundaries but with false contours. VLSBC [51] shows a better segmentation accuracy than the Zhang et al. [52] model, which has significantly more false contours. FVOD [53] and SAM [62] produce acceptable results that are visually alike, yet both struggle with computational cost compared to our method.

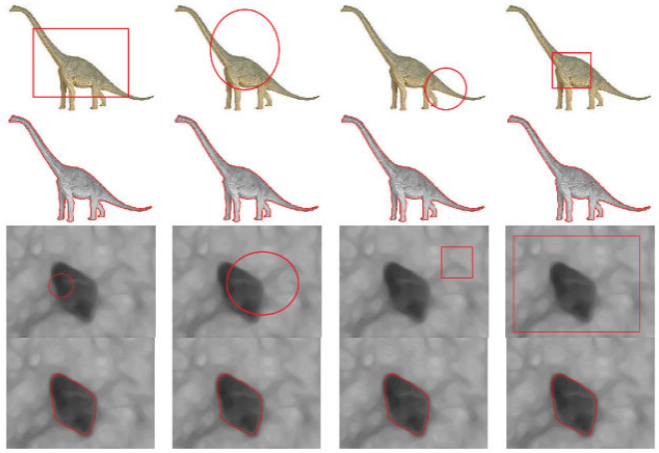

Fig. 9. Segmentation results over synthetic and real objects using the proposed model. Rows 1 and 3: input image with the initial contour of different shapes and sizes. Rows 2 and 4: results using the proposed model.

TABLE IV

CPU TIMES AND ITERATIONS FOR CONTOUR EVOLUTION OVER THE IMAGES IN FIG. 6

Method		Col 1	Col 2	Col 3
CV	Time (s)	24	33	37.63
	Iterations	500	500	500
LBF	Time (s)	22	26.67	25.32
	Iterations	500	500	500
LIF	Time (s)	7.59	9.87	15.45
	Iterations	500	500	480
VLSBC	Time (s)	15.01	8.87	13.06
	Iterations	50	17	27
Zhang et al.	Time (s)	21.32	16.73	185.9
	Iterations	50	70	65
FVOD	Time (s)	2.69	2.98	3.47
	Iterations	50	50	50
FRAGL	Time (s)	4.52	2.05	3.32
	Iterations	50	20	20
SAM	Time (s)	2.12	2.32	2.56
	Iterations	10	12	15
Proposed Model	Time (s)	1.10	1.29	1.58
	Iterations	3	3	3

Table VI lists the processing times and iterations for the image segmentation in Fig. 8 and confirms the better performance of our approach. The initial contour position for all of the in-comparison methods is set the same for each of the examples in Figs. 5–8.

Furthermore, Fig. 9 shows contours at different locations fitting over synthetic and real object images. As the initial contour is outside the ROI, it squeezes to detect ROI boundaries. It is confirmed that the proposed methodology is less sensitive to the initial position of contour as it achieved the same level of segmentation despite contour initialization of different sizes, shapes, and regions.

TABLE V
CPU TIMES AND ITERATIONS FOR CONTOUR EVOLUTION OVER THE IMAGES IN FIG. 7

Method		Col 1	Col 2	Col 3
C-V	Time (s)	1.89	3.43	7.4
	Iterations	50	100	500
LBF	Time (s)	4.74	5.74	9.21
	Iterations	40	30	26
LIF	Time (s)	4.0	4.89	5.64
	Iterations	200	500	500
VLSBC	Time (s)	3.13	2.86	1.42
	Iterations	50	50	50
Zhang et al.	Time (s)	8.64	1.41	1.37
	Iterations	50	50	50
FVOD	Time (s)	3.07	2.69	3.11
	Iterations	35	20	40
FRAGL	Time (s)	1.45	1.04	1.09
	Iterations	15	10	10
SAM	Time (s)	2.46	2.67	2.91
	Iterations	15	20	20
Proposed Model	Time (s)	1.03	0.91	0.93
	Iterations	4	2	2

TABLE VI
CPU TIMES AND ITERATIONS FOR CONTOUR EVOLUTION OVER THE IMAGES IN FIG. 8

Method		Row 1	Row 2
C-V	Time (s)	5.06	8.72
	Iterations	100	500
LBF	Time (s)	5.01	7.01
	Iterations	400	500
LIF	Time (s)	2.89	4.01
	Iterations	500	500
VLSBC	Time (s)	6.48	9.42
	Iterations	50	50
Zhang et al.	Time (s)	7.63	10.14
	Iterations	50	50
FVOD	Time (s)	3.46	3.49
	Iterations	50	50
FRAGL	Time (s)	1.21	1.65
	Iterations	7	11
SAM	Time (s)	1.96	2.07
	Iterations	8	10
Proposed Model	Time (s)	1.05	1.23
	Iterations	3	4

To add transparency to our experiments, we have added Sections IV-A–IV-C.

A. Analysis of Segmentation Accuracy

This section discusses the segmentation accuracy of the ACMs we tested based on the segmentation results over images from the PH^2 database [63] and the skin-cancer-mnist-ham10000 database [64]. Both datasets consist of dermoscopic images of possible skin lesions. Figs. 10 and 11 show the input images from both the medical datasets obtained through multiple sources, their ground truths, and the proposed ACM segmentation results.

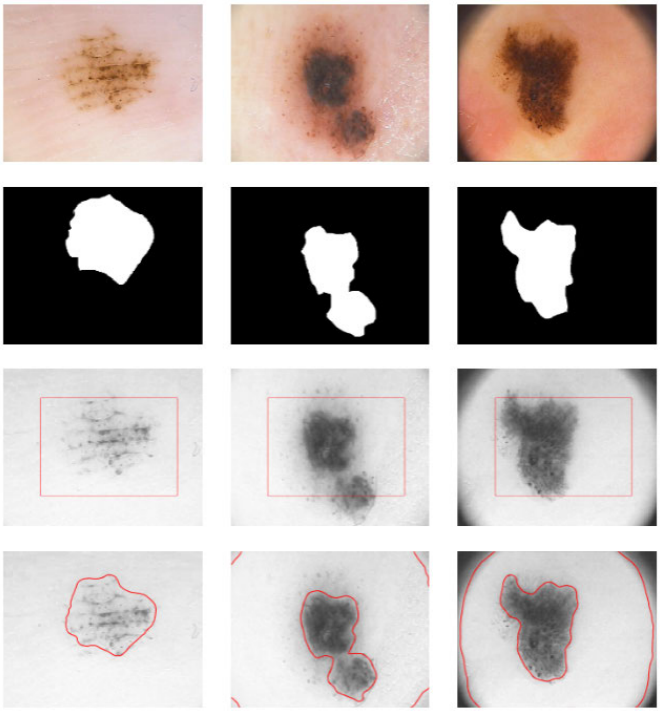

Fig. 10. Segmentation results over the sample images from the PH^2 database [63] using the proposed model. Row 1: input image. Row 2: ground truth. Row 3: initial contour. Row 4: proposed model.

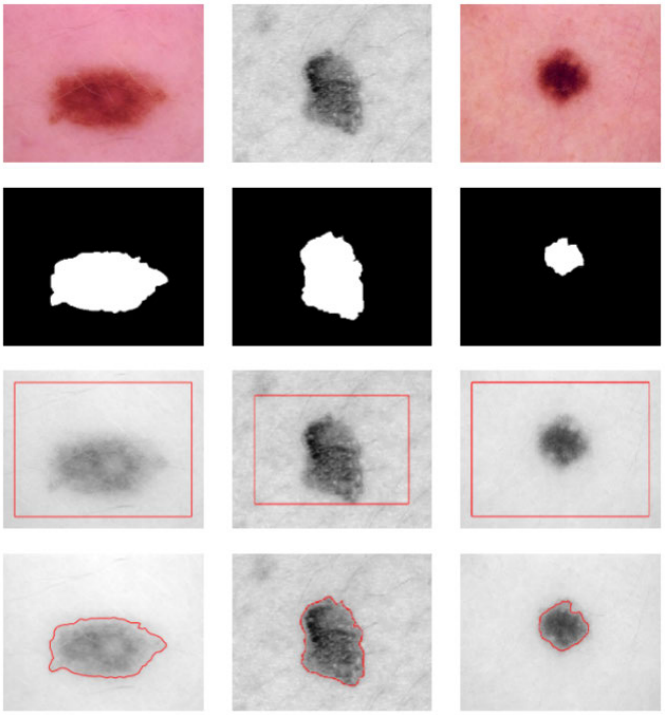

Fig. 11. Segmentation results over the sample images from the skin–cancer-mnist-ham10000 database [64] using the proposed model. Row 1: input image. Row 2: ground truth. Row 3: initial contour. Row 4: proposed model.

First, we performed the contour evolution, using the proposed methodology, over images from the PH^2 database [63], as shown in Fig. 10. The first row presents input images and the second row presents ground truths. The third and fourth rows show the initial contour position over input images and the final segmentation results, respectively. Visual analysis

approves that the contour has successfully detected the object boundaries.

The skin-cancer-mnist-ham10000 database contains about 10 000 images; the proposed model is tested on 25% of the total images, randomly selected, from the database [64]. Fig. 11 presents the results generated by the proposed methodology over sample images from the skin-cancer-mnist-ham10000 database [64]. The first row contains input images, followed by ground truths in the second row. The third and fourth rows show the initial contour position over input images and the final segmentation results, respectively. From the visual analysis, it is approved that the contour is fully tied to the object boundaries.

The segmentation result produced using our methodology is compared with previous ACM methods against respective ground truths to calculate its accuracy.

The segmentation accuracy is defined as

$$\text{Accuracy}_{\text{segm}} = \frac{\text{TP} + \text{TN}}{\text{TP} + \text{TN} + \text{FP} + \text{FN}} \tag{40}$$

which is the closeness between the produced segmentation results and their respective ground truths.

We also measured the Dice index and sensitivity over both datasets mentioned above. The Dice index gives the similarity of two samples: the segmentation result and the ground truth in our case. The sensitivity is the measure of how much the detected region belongs to the actual region. The mathematical formulation for the Dice index and sensitivity is

$$\text{Dice}_{\text{seg}} = \frac{2 \times \text{TP}}{2 \times \text{TP} + \text{FP} + \text{FN}} \tag{41}$$

and

$$\text{Sens}_{\text{seg}} = \frac{\text{TP}}{\text{TP} + \text{FN}} \tag{42}$$

respectively.

TP, TN, FP, and FN account for true positive, true negative, false positive, and false negative terms, respectively. TP shows the segmented actual regions, TN shows the correctly nonsegmented regions, FP shows the detected false regions, and FN shows the undetected actual regions. In the context of segmentation, these metrics help evaluate the segmentation models against the respective ground truths of objects to be segmented in given images. These values are calculated at pixel levels. The results are considered good if $\text{Accuracy}_{\text{segm}}$ has a value near to 1 and poor if the value is near 0.

Tables VII and VIII give the quantitative values for segmentation quality analysis over both the mentioned databases; all of these values are measured based on test results of various ACMs. Fig. 12 shows the graphical representation of Tables VII and VIII. This analysis of both the experimented datasets exhibits the superiority of the proposed edge-based local and global energy active contours model.

To add transparency to Section IV, we further evaluated previous models and our model on the THUS10000 dataset [65]. This time we used F-measure given as

$$\text{F-measure} = 2\frac{(P \times R)}{P + R}\% \tag{43}$$

where $P = (|S \cap G|/|S|)$ and $R = (|S \cap G|/|G|)$ are the precision and sensitivity, respectively. F-measure for the segmentation results of THUS10000 [65] method along with the average time taken for segmenting one image is shown in Table IX and Fig. 13. The top row in Fig. 13 shows the input images with initial contours of different shapes and sizes, followed by the corresponding ground truths. The third, fourth, fifth, and sixth rows contain the segmentation results of the FVOD [53], FRAGL [61], SAM [62], and the proposed model, respectively.

Although all the comparison methods show reasonable performance, the results presented in Table IX confirm that the proposed method outclasses previous methods regarding computational time and F-measure.

TABLE VII

ANALYSIS OF SEGMENTATION ACCURACY OF THE PH^2 DATABASE [63]

Methods	Accuracy	Sensitivity	Dice Index
CV	0.6678	0.6779	0.5063
LBF	0.8441	0.7887	0.7797
LIF	0.8641	0.8136	0.8331
VLSBC	0.8937	0.7839	0.8776
Zhang et al.	0.9140	0.9135	0.8740
FVOD	0.9332	0.9468	0.9412
FRAGL	0.9668	0.9637	0.9602
SAM	0.9701	0.9689	0.9739
Proposed Method	0.9768	0.9729	0.9771

TABLE VIII

ANALYSIS OF SEGMENTATION ACCURACY OF THE SKIN-CANCER-MNIST-HAM10000 [64] DATABASE

Methods	Accuracy	Sensitivity	Dice Index
CV	0.6599	0.6872	0.5383
LBF	0.8359	0.7949	0.8009
LIF	0.8521	0.8234	0.8257
VLSBC	0.8967	0.8136	0.8879
Zhang et al.	0.9395	0.9360	0.8937
FVOD	0.9651	0.9649	0.9609
FRAGL	0.9721	0.9698	0.9631
SAM	0.9801	0.9732	0.9789
Proposed Method	0.9878	0.9843	0.9881

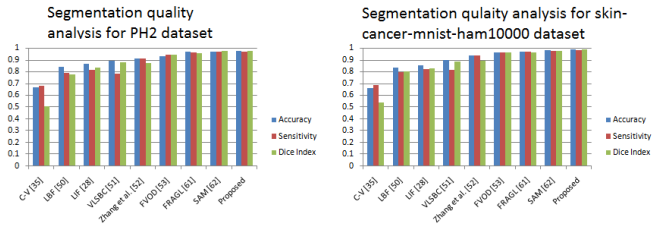

Fig. 12. Graphical representation of segmentation quality analysis for the proposed method and previous methods. Left: PH^2 database [63]. Right: skin-cancer-mnist-ham10000 [64].

TABLE IX

F-MEASURE AND AVERAGE CPU TIME OF SEGMENTATION RESULTS FOR THUS10000 DATASET [65]

Metric / CPU Time (sec)	FVOD	FRAGL	SAM	Proposed Method
F-measure	0.7418	0.8236	0.8457	0.8898
Time (s)	10.89	3.05	2.90	1.89

B. Noise Sensitivity Analysis

This section discusses the robustness of the proposed method when the images are corrupted with varying noise levels. We use the Jaccard similarity index (JSI) to compare

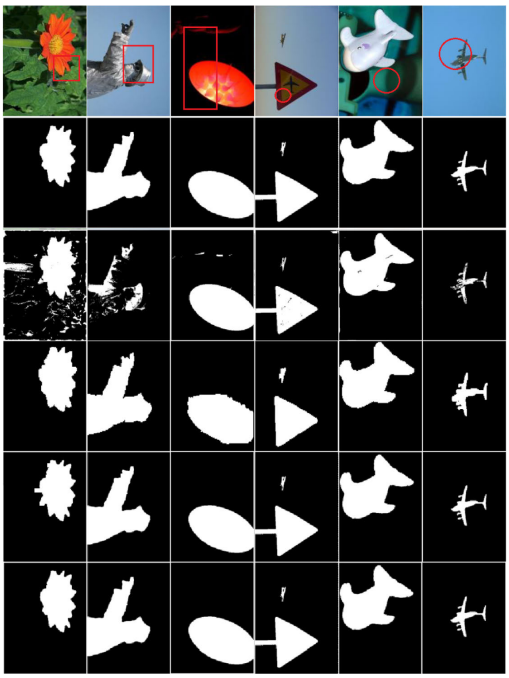

Fig. 13. Segmentation results over sample images from the THUS10000 dataset [65]. Row 1: input image with initial contours of different shapes and sizes. Row 2: ground truth. Row 3: FVOD [53] segmentation results. Row 4: FRAGL [61] segmentation results. Row 5: SAM [62] segmentation results. Row 6: proposed model segmentation results.

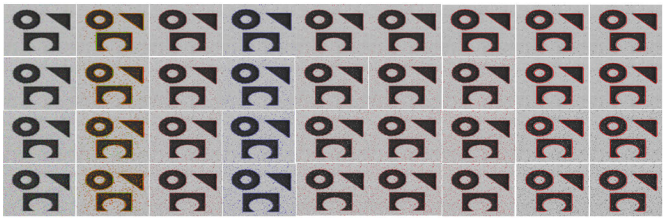

Fig. 14. Column 1: input image corrupted with salt and pepper noise levels (0.01, 0.02, 0.03, 0.04, and 0.05). Column 2: C-V [35]. Column 3: LBF [50]. Column 4: LIF [28]. Column 5: VLSBC [51]. Column 6: FVOD [53]. Column 7: FRAGL [61]. Column 8: SAM [62]. Column 9: proposed model.

our results with the corresponding ground truths to perform noise sensitivity analysis. JSI computes the intersection of the segmentation result and the related ground truth divided by the union of both. JSI is given as

$$\mathrm{JSI}(S, G) = \frac{|S \cap G|}{|S \cup G|} \tag{44}$$

where S and G are the segmentation result and the corresponding ground truth, respectively.

Figs. 14 and 15 show the segmentation results of various ACM models, including the proposed model over an image with different levels of salt and pepper and Gaussian artificial noises (0.01, 0.02, 0.03, and 0.04) in Rows 1–4, respectively. Figs. 14 and 15 show that the global region-based models struggle to capture object boundaries with the increase in noise levels, producing false contours as well. For Gaussian noise, Fang et al. [61] made no false contours and captured the entire object of interest. However, the proposed model captured the object of interest without false contours irrespective of the noise type and given noise levels. The segmentation accuracy compared against the ground truth of the given case is shown

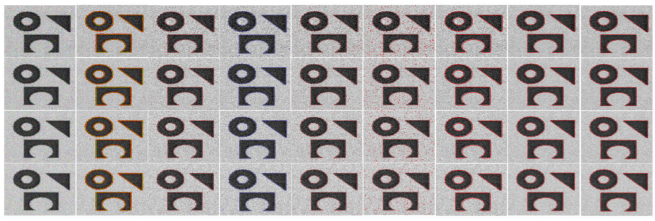

Fig. 15. Column 1: input image corrupted with Gaussian noise levels (0.01, 0.02, 0.03, 0.04, and 0.05). Column 2: C-V [35]. Column 3: LBF [50]. Column 4: LIF [28]. Column 5: VLSBC [51]. Column 6: FVOD [53]. Column 7: FRAGL [61]. Column 8: SAM [62]. Column 9: proposed model.

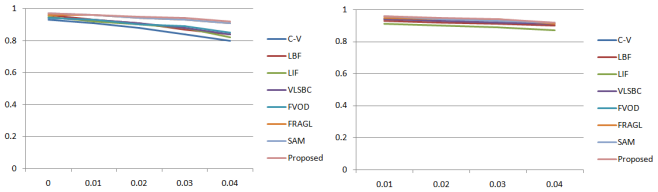

Fig. 16. From left to right: JSI values for Figs. 14 and 15.

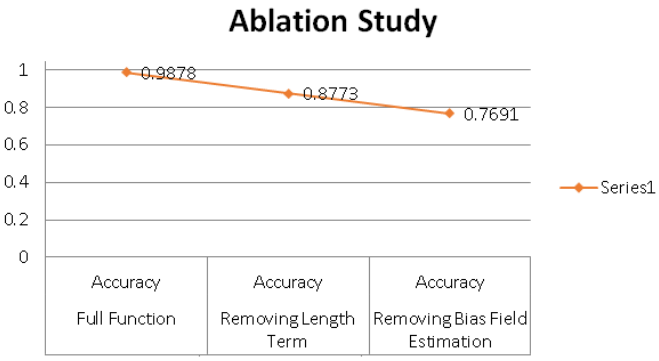

Fig. 17. Ablation study over PH^2 database by removing features from the proposed function.

by the JSI chart in Fig. 16, confirming the robustness of the proposed model against noise.

C. Ablation Study

This section presents the ablation study to verify the contribution of subfunctions included in the proposed model. The ablation study is conducted against the segmentation accuracy metric on the PH^2 database only. Our model consists of statistical information of the global and local regions enforced by the SPF function. It also deals with inhomogeneity by introducing bias field estimation in it. Each of these functions has its impact in terms of improving the performance of our model. We will be removing some of the features to observe their effects on the overall performance. First, we will be removing L_{spf}, the region-based length term derived by the spf function, from (21) to observe its influence on the overall methodology. L_{spf} is calculated based on the spf function; therefore, the solution starts getting stuck in local minima, which significantly degrades its performance. Furthermore, false contours begin to appear with iterations degrading the correctness of the method.

Fig. 18. Comparing segmentation performance of DeepLabV3+ and the proposed method. Top row: input images. Row 2: DeepLabV3+ [54] segmentation results. Row 3: input image with initial contours of random shapes and sizes for each. Row 4: proposed method segmentation results.

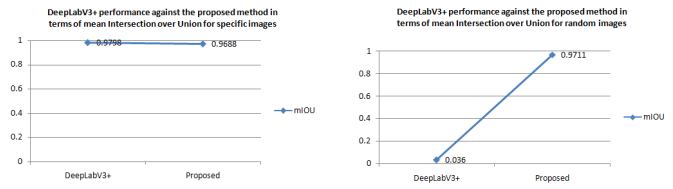

Fig. 19. Evaluation indicator for DeepLabV3+ [54] and the proposed method. Left: DeepLabV3+ performance against the proposed method in terms of mean IOU for specific images. Right: DeepLabV3+ performance against the proposed method in terms of mean IOU for random images.

In the second step, we remove $b(x)$, the bias field estimation process, and observe its impact on the proposed method's performance.

Fig. 17 shows the presentation of the ablation study over PH^2 database by removing the length term and the bias field estimation process from the proposed function. It is deduced that each of the features contributes to achieving higher accuracy and hence is essential for computing better segmentation results.

V. Discussion

This research presents a new hybrid ACM comprising local and global statistical information of images enforced by an SPF function. All of these features contribute to better segmentation quality, which is further analyzed by the ablation studies. Deep learning-based techniques are widely adopted for segmentation these days; however, their performance significantly relies on the dataset size. That said, the choice of segmentation technique depends on factors, such as the specific application, available data, computational resources, and desired level of accuracy [66]. While deep learning methods dominate many areas of image segmentation, traditional segmentation techniques can still be useful in scenarios where deep learning might not be suitable or when interpretability and simplicity are essential. The higher the dataset, the better the segmentation quality, which is not good when dealing with comparatively small datasets. Contrarily, the proposed model belongs to the category of unsupervised methods that do not depend on the size of the dataset and can be more useful on small datasets compared with supervised settings.

We further compared the proposed method with DeepLabV3+ [54], an SOTA deep learning-based method, to reaffirm that our traditional segmentation technique is superior in scenarios with no or less training data. Fig. 18 presents the segmentation results when the [54] model and the proposed models segment specific images (Columns 1–4) from the Pascal VOC dataset [67] and random images (Columns 5–8). Results show that work [54] produces superior results when tested on specific images, while it segments only part of the ROI in random images, which is often wrong too. On the other hand, the proposed technique produces results within a desirable range for both the specific and random images; moreover, it surpasses the work [54] over random images. Fig. 19 presents the evaluation indicator, intersection over union (IOU), for DeepLabV3+ and the proposed method for specific and random images.

VI. Conclusion

This study comes up with a jointly formed energy fitting function, including the local and global fit models for intensity corrupted or inhomogeneous image segmentation. The bias field is adjoined with the local-region-based fit energy in this energy function; it increases the efficacy of the proposed methodology over inhomogeneous regions. An spf function drives the region-based length term to assist the contour in whether to evolve inner or outer direction. The local and global energy functions are integrated to build up their combined effect, further joined with the edge-indicator function—the inclusion of edge-indicator function speedups contour over objects with sharp edges. Section IV contains a comparison of the proposed model with previous ACMs against various performance metrics. The analysis of the segmentation based on the PH^2, skin-cancer-mnist-ham10000, and THUS10000 databases approves the superior achievement of the proposed model. Finally, we discuss the usability and applicability cases of our approach when a deep learning-based model compromises its performance.

REFERENCES

[1] M. Drozdzal et al., "Learning normalized inputs for iterative estimation in medical image segmentation," *Med. Image Anal.*, vol. 44, pp. 1–13, Feb. 2018.

[2] C. Liu, M. K.-P. Ng, and T. Zeng, "Weighted variational model for selective image segmentation with application to medical images," *Pattern Recognit.*, vol. 76, pp. 367–379, Apr. 2018.

[3] E. Romera, J. M. Álvarez, L. M. Bergasa, and R. Arroyo, "ERFNet: Efficient residual factorized ConvNet for real-time semantic segmentation," *IEEE Trans. Intell. Transp. Syst.*, vol. 19, no. 1, pp. 263–272, Jan. 2018.

[4] Y. Zhang, Y. Su, J. Yang, J. Ponce, and H. Kong, "When Dijkstra meets vanishing point: A stereo vision approach for road detection," *IEEE Trans. Image Process.*, vol. 27, no. 5, pp. 2176–2188, May 2018.

[5] B. Gao, X. Li, W. L. Woo, and G. Y. Tian, "Physics-based image segmentation using first order statistical properties and genetic algorithm for inductive thermography imaging," *IEEE Trans. Image Process.*, vol. 27, no. 5, pp. 2160–2175, May 2018.

[6] C. Liu, Y. Xiao, and J. Yang, "A coastline detection method in polarimetric SAR images mixing the region-based and edge-based active contour models," *IEEE Trans. Geosci. Remote Sens.*, vol. 55, no. 7, pp. 3735–3747, Jul. 2017.

[7] J. Long, E. Shelhamer, and T. Darrell, "Fully convolutional networks for semantic segmentation," in *Proc. IEEE Conf. Comput. Vis. Pattern Recognit. (CVPR)*, Jun. 2015, pp. 3431–3440.

[8] L.-C. Chen, G. Papandreou, I. Kokkinos, K. Murphy, and A. L. Yuille, "DeepLab: Semantic image segmentation with deep convolutional nets, atrous convolution, and fully connected CRFs," *IEEE Trans. Pattern Anal. Mach. Intell.*, vol. 40, no. 4, pp. 834–848, Apr. 2018.

[9] B. Kang, Y. Lee, and T. Q. Nguyen, "Depth-adaptive deep neural network for semantic segmentation," *IEEE Trans. Multimedia*, vol. 20, no. 9, pp. 2478–2490, Sep. 2018.

[10] J. Liu, Y. Wang, Y. Li, J. Fu, J. Li, and H. Lu, "Collaborative deconvolutional neural networks for joint depth estimation and semantic segmentation," *IEEE Trans. Neural Netw. Learn. Syst.*, vol. 29, no. 11, pp. 5655–5666, Nov. 2018.

[11] B. Shuai, Z. Zuo, G. Wang, and B. Wang, "Scene parsing with integration of parametric and non-parametric models," *IEEE Trans. Image Process.*, vol. 25, no. 5, pp. 2379–2391, May 2016.

[12] S. Bu, P. Han, Z. Liu, and J. Han, "Scene parsing using inference embedded deep networks," *Pattern Recognit.*, vol. 59, pp. 188–198, Nov. 2016.

[13] R. Zhang, L. Lin, G. Wang, M. Wang, and W. Zuo, "Hierarchical scene parsing by weakly supervised learning with image descriptions," *IEEE Trans. Pattern Anal. Mach. Intell.*, vol. 41, no. 3, pp. 596–610, Mar. 2019.

[14] H. Shi, H. Li, F. Meng, Q. Wu, L. Xu, and K. N. Ngan, "Hierarchical parsing net: Semantic scene parsing from global scene to objects," *IEEE Trans. Multimedia*, vol. 20, no. 10, pp. 2670–2682, Oct. 2018.

[15] A. Tiwari, S. Srivastava, and M. Pant, "Brain tumor segmentation and classification from magnetic resonance images: Review of selected methods from 2014 to 2019," *Pattern Recognit. Lett.*, vol. 131, pp. 244–260, Mar. 2020.

[16] M. Kass, A. Witkin, and D. Terzopoulos, "Snakes: Active contour models," *Int. J. Comput. Vis.*, vol. 1, no. 4, pp. 321–331, Jan. 1988.

[17] V. Caselles, F. Catté, T. Coll, and F. Dibos, "A geometric model for active contours in image processing," *Numerische Math.*, vol. 66, no. 1, pp. 1–31, Dec. 1993.

[18] R. Goldenberg, R. Kimmel, E. Rivlin, and M. Rudzsky, "Fast geodesic active contours," *IEEE Trans. Image Process.*, vol. 10, no. 10, pp. 1467–1475, Oct. 2001.

[19] C. Li, C. Xu, C. Gui, and M. D. Fox, "Distance regularized level set evolution and its application to image segmentation," *IEEE Trans. Image Process.*, vol. 19, no. 12, pp. 3243–3254, Dec. 2010.

[20] C. Li, C. Xu, C. Gui, and M. D. Fox, "Level set evolution without re-initialization: A new variational formulation," in *Proc. IEEE Comput. Soc. Conf. Comput. Vis. Pattern Recognit.*, Jun. 2005, pp. 430–436.

[21] V. Caselles, R. Kimmel, and G. Sapiro, "Geodesic active contours," *Int. J. Comput. Vis.*, vol. 22, no. 1, pp. 61–79, 1997.

[22] B. Zhou and C.-L. Mu, "Level set evolution for boundary extraction based on a p-Laplace equation," *Appl. Math. Model.*, vol. 34, no. 12, pp. 3910–3916, Dec. 2010.

[23] C. Huang and L. Zeng, "Level set evolution model for image segmentation based on variable exponent p-Laplace equation," *Appl. Math. Model.*, vol. 40, nos. 17–18, pp. 7739–7750, Sep. 2016.

[24] Y. Wang and C. He, "Adaptive level set evolution starting with a constant function," *Appl. Math. Model.*, vol. 36, no. 7, pp. 3217–3228, Jul. 2012.

[25] S. Lankton and A. Tannenbaum, "Localizing region-based active contours," *IEEE Trans. Image Process.*, vol. 17, no. 11, pp. 2029–2039, Nov. 2008.

[26] L. Wang, Y. Chang, H. Wang, Z. Wu, J. Pu, and X. Yang, "An active contour model based on local fitted images for image segmentation," *Inf. Sci.*, vols. 418–419, pp. 61–73, Dec. 2017.

[27] C. Li, C.-Y. Kao, J. C. Gore, and Z. Ding, "Minimization of region-scalable fitting energy for image segmentation," *IEEE Trans. Image Process.*, vol. 17, no. 10, pp. 1940–1949, Oct. 2008.

[28] K. Zhang, H. Song, and L. Zhang, "Active contours driven by local image fitting energy," *Pattern Recognit.*, vol. 43, no. 4, pp. 1199–1206, Apr. 2010.

[29] A. Joshi, M. S. Khan, A. Niaz, F. Akram, H. C. Song, and K. N. Choi, "Active contour model with adaptive weighted function for robust image segmentation under biased conditions," *Expert Syst. Appl.*, vol. 175, Aug. 2021, Art. no. 114811.

[30] M. F. Talu, "ORACM: Online region-based active contour model," *Expert Syst. Appl.*, vol. 40, no. 16, pp. 6233–6240, Nov. 2013.

[31] X. Jiang, B. Li, Q. Wang, and P. Chen, "A novel active contour model driven by local and global intensity fitting energies," *Optik*, vol. 125, no. 21, pp. 6445–6449, Nov. 2014.

[32] J. Oh, D. R. Martin, and X. Hu, "Partitioned edge-function-scaled region-based active contour (p-ESRAC): Automated liver segmentation in multiphase contrast-enhanced MRI," *Med. Phys.*, vol. 41, no. 4, Apr. 2014, Art. no. 041914.

[33] S. Liu and Y. Peng, "A local region-based Chan–Vese model for image segmentation," *Pattern Recognit.*, vol. 45, no. 7, pp. 2769–2779, Jul. 2012.

[34] H. Wang, T.-Z. Huang, Z. Xu, and Y. Wang, "An active contour model and its algorithms with local and global Gaussian distribution fitting energies," *Inf. Sci.*, vol. 263, pp. 43–59, Apr. 2014.

[35] T. F. Chan and L. A. Vese, "Active contours without edges," *IEEE Trans. Image Process.*, vol. 10, no. 2, pp. 266–277, Feb. 2001.

[36] S. Soomro, F. Akram, J. H. Kim, T. A. Soomro, and K. N. Choi, "Active contours using additive local and global intensity fitting models for intensity inhomogeneous image segmentation," *Comput. Math. Methods Med.*, vol. 2016, pp. 1–15, Jan. 2016.

[37] S. Soomro, A. Munir, and K. N. Choi, "Hybrid two-stage active contour method with region and edge information for intensity inhomogeneous image segmentation," *PLoS ONE*, vol. 13, no. 1, Jan. 2018, Art. no. e0191827.

[38] L. Wang, C. Li, Q. Sun, D. Xia, and C.-Y. Kao, "Active contours driven by local and global intensity fitting energy with application to brain MR image segmentation," *Computerized Med. Imag. Graph.*, vol. 33, no. 7, pp. 520–531, Oct. 2009.

[39] A. Munir, S. Soomro, C. H. Lee, and K. N. Choi, "Adaptive active contours based on variable kernel with constant initialisation," *IET Image Process.*, vol. 12, no. 7, pp. 1117–1123, Jul. 2018.

[40] S. Soomro, F. Akram, A. Munir, C. H. Lee, and K. N. Choi, "Segmentation of left and right ventricles in cardiac MRI using active contours," *Comput. Math. Methods Med.*, vol. 2017, pp. 1–16, Jan. 2017.

[41] A. Niaz et al., "Hybrid active contour based on local and global statistics parameterized by weight coefficients for inhomogeneous image segmentation," *IEEE Access*, vol. 8, pp. 57348–57362, 2020.

[42] B. Wang, X. Gao, D. Tao, and X. Li, "A nonlinear adaptive level set for image segmentation," *IEEE Trans. Cybern.*, vol. 44, no. 3, pp. 418–428, Mar. 2014.

[43] H. Ali, L. Rada, and N. Badshah, "Image segmentation for intensity inhomogeneity in presence of high noise," *IEEE Trans. Image Process.*, vol. 27, no. 8, pp. 3729–3738, Aug. 2018.

[44] Z. Ji, Y. Xia, Q. Sun, G. Cao, and Q. Chen, "Active contours driven by local likelihood image fitting energy for image segmentation," *Inf. Sci.*, vol. 301, pp. 285–304, Apr. 2015.

[45] H. Min, W. Jia, Y. Zhao, W. Zuo, H. Ling, and Y. Luo, "LATE: A level-set method based on local approximation of Taylor expansion for segmenting intensity inhomogeneous images," *IEEE Trans. Image Process.*, vol. 27, no. 10, pp. 5016–5031, Oct. 2018.

[46] S. Niu, Q. Chen, L. de Sisternes, Z. Ji, Z. Zhou, and D. L. Rubin, "Robust noise region-based active contour model via local similarity factor for image segmentation," *Pattern Recognit.*, vol. 61, pp. 104–119, Jan. 2017.

[47] J. Zhang, Z. Lu, and M. Li, "Active contour-based method for finger-vein image segmentation," *IEEE Trans. Instrum. Meas.*, vol. 69, no. 11, pp. 8656–8665, Nov. 2020.

[48] G. Wang, F. Zhang, Y. Chen, G. Weng, and H. Chen, "An active contour model based on local pre-piecewise fitting bias corrections for fast and accurate segmentation," *IEEE Trans. Instrum. Meas.*, vol. 72, pp. 1–13, 2023.

[49] D. Mumford and J. Shah, "Optimal approximations by piecewise smooth functions and associated variational problems," *Commun. Pure Appl. Math.*, vol. 42, no. 5, pp. 577–685, Jul. 1989.

[50] C. Li, R. Huang, Z. Ding, J. C. Gatenby, D. N. Metaxas, and J. C. Gore, "A level set method for image segmentation in the presence of intensity inhomogeneities with application to MRI," *IEEE Trans. Image Process.*, vol. 20, no. 7, pp. 2007–2016, Jul. 2011.

[51] K. Zhang, Q. Liu, H. Song, and X. Li, "A variational approach to simultaneous image segmentation and bias correction," *IEEE Trans. Cybern.*, vol. 45, no. 8, pp. 1426–1437, Aug. 2015.

[52] K. Zhang, L. Zhang, K.-M. Lam, and D. Zhang, "A level set approach to image segmentation with intensity inhomogeneity," *IEEE Trans. Cybern.*, vol. 46, no. 2, pp. 546–557, Feb. 2016.

[53] Y. Zhang and Y. Tian, "A new active contour medical image segmentation method based on fractional varying-order differential," *Mathematics*, vol. 10, no. 2, p. 206, Jan. 2022.

[54] L.-C. Chen, Y. Zhu, G. Papandreou, F. Schroff, and H. Adam, "Encoder–decoder with Atrous separable convolution for semantic image segmentation," in *Proc. Eur. Conf. Comput. Vis. (ECCV)*, 2018, pp. 801–818.

[55] Y. Yu et al., "Techniques and challenges of image segmentation: A review," *Electronics*, vol. 12, no. 5, p. 1199, Mar. 2023.

[56] A. Khadidos, V. Sanchez, and C.-T. Li, "Active contours based on weighted gradient vector flow and balloon forces for medical image segmentation," in *Proc. IEEE Int. Conf. Image Process. (ICIP)*, Oct. 2014, pp. 902–906.

[57] L. Fang, T. Qiu, H. Zhao, and F. Lv, "A hybrid active contour model based on global and local information for medical image segmentation," *Multidimensional Syst. Signal Process.*, vol. 30, no. 2, pp. 689–703, Apr. 2019.

[58] L. Sun, X. Meng, J. Xu, and Y. Tian, "An image segmentation method using an active contour model based on improved SPF and LIF," *Appl. Sci.*, vol. 8, no. 12, p. 2576, Dec. 2018.

[59] B. Han and Y. Wu, "Active contours driven by global and local weighted signed pressure force for image segmentation," *Pattern Recognit.*, vol. 88, pp. 715–728, Apr. 2019.

[60] G. Aubert, P. Kornprobst, and G. Aubert, *Mathematical Problems in Image Processing: Partial Differential Equations and the Calculus of Variations*, vol. 147. Cham, Switzerland: Springer, 2006.

[61] J. Fang, H. Liu, L. Zhang, J. Liu, and H. Liu, "Fuzzy region-based active contours driven by weighting global and local fitting energy," *IEEE Access*, vol. 7, pp. 184518–184536, 2019.

[62] A. Fallahdizcheh, S. Laroia, and C. Wang, "Sequential active contour based on morphological-driven thresholding for ultrasound image segmentation of ascites," *IEEE J. Biomed. Health Informat.*, vol. 27, no. 9, pp. 4305–4316, Sep. 2023.

[63] T. Mendonça, P. M. Ferreira, J. S. Marques, A. R. Marcal, and J. Rozeira, "PH^2—A dermoscopic image database for research and benchmarking," in *Proc. 35th Annu. Int. Conf. IEEE Eng. Med. Biol. Soc. (EMBC)*, Jul. 2013, pp. 5437–5440.

[64] P. Tschandl, C. Rosendahl, and H. Kittler, "The HAM10000 dataset, a large collection of multi-source dermatoscopic images of common pigmented skin lesions," *Sci. Data*, vol. 5, no. 1, pp. 1–9, Aug. 2018.

[65] M.-M. Cheng, N. J. Mitra, X. Huang, P. H. S. Torr, and S.-M. Hu, "Global contrast based salient region detection," *IEEE Trans. Pattern Anal. Mach. Intell.*, vol. 37, no. 3, pp. 569–582, Mar. 2015.

[66] S. U. Amin, A. Hussain, B. Kim, and S. Seo, "Deep learning based active learning technique for data annotation and improve the overall performance of classification models," *Expert Syst. Appl.*, vol. 228, Oct. 2023, Art. no. 120391.

[67] M. Everingham, L. Van Gool, C. K. I. Williams, J. Winn, and A. Zisserman, "The PASCAL visual object classes challenge 2007 (VOC2007) results," [Online]. Available: http://www.pascalnetwork.org/challenges/VOC/voc2007/workshop/index.html

Asim Niaz received the B.S. degree in electrical (computer) engineering from the COMSATS Institute of Information Technology, Islamabad, Pakistan, in 2016, and the M.S. degree in computer science and engineering from Chung-Ang University, Seoul, South Korea, in 2020.

He worked as a Research Assistant at the Visual Image Media Laboratory, Seoul. Later, he visited INRIA Sophia Antipolis, Biot, France, followed by his research internship at Ericsson Canada, Mississauga, ON, Canada. He is currently a Research Assistant at the AI Vision Laboratory, Seoul. His current research interests include action recognition, video understanding, anomaly detection in images and videos, medical image analysis, and image segmentation.

Ehtesham Iqbal received the B.S. degree in electrical (computer) engineering from the COMSATS Institute of Information Technology, Islamabad, Pakistan, in 2017, and the M.S. degree from the Department of Computer Science and Engineering, Chung-Ang University, Seoul, South Korea, in 2021.

He worked as a Research Assistant at the Visual Image Media Laboratory. His research interests include medical image analysis and semantic segmentation.

Asif Aziz Memon received the B.E. and M.E. degrees from Mehran UET, Jamshoro, Pakistan, in 2010 and 2015, respectively, and the Ph.D. degree in application software from Chung-Ang University, Seoul, South Korea, in 2021.

His research interests include image segmentation, image recognition, and medical imaging.

Asad Munir received the bachelor's degree in engineering sciences from the Ghulam Ishaq Khan Institute of Engineering Sciences and Technology, Topi, Pakistan, in 2013, the master's degree in computer science from Chung-Ang University, Seoul, South Korea, in 2018, and the Ph.D. degree from the Department of Industrial and Information Engineering, Università degli Studi di Udine, Udine, Italy, in 2022.

His current research interests include object segmentation, object tracking, and person reidentification.

Jin Kim received the B.S. and M.S. degrees in computer science and engineering from Chung-Ang University, Seoul, South Korea, in 2014 and 2016, respectively.

He is currently a Lead Software Engineer at SecuLayer, Inc., Seoul. His research interests include auto machine learning, artificial intelligence, and big data artificial intelligence (AI) platform.

Kwang Nam Choi received the B.S. and M.S. degrees from the Department of Computer Science, Chung-Ang University, Seoul, South Korea, in 1988 and 1990, respectively, and the Ph.D. degree in computer science from the University of York, York, U.K., in 2002.

He is currently a Professor with the School of Computer Science and Engineering, Chung-Ang University. His current research interests include motion tracking, object categorization, and 3-D image recognition.